Jet–Topography Interactions Affect Energy Pathways to the Deep Southern Ocean

ALICE BARTHEL

Climate Change Research Centre, and ARC Centre of Excellence for Climate System Science, University of New South Wales, Sydney, New South Wales, Australia

ANDREW MCC. HOGG

Research School of Earth Sciences, and ARC Centre of Excellence for Climate System Science, Australian National University, Canberra, Australian Capital Territory, Australia

STEPHANIE WATERMAN

Department of Earth, Ocean, and Atmospheric Sciences, University of British Columbia, Vancouver, British Columbia, Canada

SHANE KEATING

School of Mathematics and Statistics, University of New South Wales, Sydney, New South Wales, Australia

(Manuscript received 28 September 2016, in final form 21 March 2017)

ABSTRACT

In the Southern Ocean, strong eastward ocean jets interact with large topographic features, generating eddies that feed back onto the mean flow. Deep-reaching eddies interact with topography, where turbulent dissipation and generation of internal lee waves play an important role in the ocean's energy budget. However, eddy effects in the deep ocean are difficult to observe and poorly characterized. This study investigates the energy contained in eddies at depth, when an ocean jet encounters topography. This study uses a two-layer ocean model in which an imposed unstable jet encounters a topographic obstacle (either a seamount or a meridional ridge) in a configuration relevant to an Antarctic Circumpolar Current frontal jet. The authors find that the presence of topography increases the eddy kinetic energy (EKE) at depth but that the dominant processes generating this deep EKE depend on the shape and height of the obstacle as well as on the baroclinicity of the jet before it encounters topography. In cases with high topography, horizontal shear instability is the dominant source of deep EKE, while a flat bottom or a strongly sheared inflow leads to deep EKE being generated primarily through baroclinic instability. These results suggest that the deep EKE is set by an interplay between the inflowing jet properties and topography and imply that the response of deep EKE to changes in the Southern Ocean circulation is likely to vary across locations depending on the topography characteristics.

1. Introduction

Southern Ocean dynamics impact the distribution of heat, salt, and nutrients in the global ocean, thus affecting climate and fisheries worldwide (Rintoul and Naveira Garabato 2013). These dynamics also play an essential role in air–sea fluxes of CO_2 (Le Quéré et al. 2007). The circulation in the Southern Ocean is expected to change in a warming climate through the combined effects of changes in freshwater fluxes (Downes and Hogg 2013) and a projected increase, and possible southern shift, in westerly winds over the region (Bracegirdle et al. 2013). Understanding the physical processes governing Southern Ocean dynamics is essential to adequately representing them in ocean models and to predicting ocean feedback on future climate.

Southern Ocean circulation is characterized by complex, multiscale interactions between ocean jets, a highly energetic mesoscale eddy field, and bottom topography. Ocean jets are narrow, fast-flowing currents. They are prevalent in the Southern Ocean, where multiple eastward-flowing jets form the Antarctic Circumpolar Current (ACC). The major frontal jets of the ACC typically measure $O(100)$ km in width and feature velocities

Corresponding author: Alice Barthel, a.barthel@unsw.edu.au

DOI: 10.1175/JPO-D-16-0220.1

of $O(0.1–1)\,\mathrm{m\,s^{-1}}$ (Waterman et al. 2013; Firing et al. 2011). Zonal jets are a robust feature of self-organized, two-dimensional turbulence on a β plane (Rhines 1975), suggesting jetlike features are likely to spontaneously emerge from an eddying flow. However, Southern Ocean jets are also affected by external factors, including wind, buoyancy forcing, and bottom topography.

The eddy field in the Southern Ocean is one of the most energetic in the world (Fu et al. 2010). These eddies transport tracers, momentum, and potential vorticity, thus playing an important role in the circulation dynamics (Vallis 2006). Eddies are traditionally viewed as deriving from the instability properties of the mean flow. Once they develop, eddies release available potential energy (APE) contained in sloping isopycnals through baroclinic processes (e.g., Karsten et al. 2002) and convert mean flow kinetic energy (KE) to eddy kinetic energy through barotropic processes, thus reducing the horizontal shear of sharp, narrow flows (e.g., Waterman and Jayne 2011). However, eddies also sustain the mean flow through the convergence of eddy momentum fluxes (e.g., Starr 1968) and can transfer energy to other eddies through nonlinear interactions, thus sustaining eddy growth in regions where the mean flow properties alone cannot support it (e.g., Chapman et al. 2015). The active eddy field in the Southern Ocean has a number of important implications for climate. The combination of large-scale forcing and local eddy effects effectively sets the vertical structure of the ACC. Eddies can also lead to strong, localized mixing of tracers across Southern Ocean fronts, which makes a significant contribution to the large-scale meridional flux of heat, carbon, and nutrients (Naveira Garabato et al. 2011; Thompson and Sallée 2012; Dufour et al. 2015). The eddy-induced mixing along isopycnals may also be an important process in the upwelling of intermediate and deep waters, providing a quasi-adiabatic route to the surface and contributing to the closure of the upper and lower cells of the meridional overturning circulation (Marshall and Speer 2012).

The mean flow and the eddy field are both constrained by bottom topography. In the Southern Ocean, the path of the ACC encounters a variety of topographic features, including large plateaus, fracture zones, ridges, and abyssal plains. To the first order, large-scale ocean currents tend to follow contours of constant f/H (with f as the Coriolis frequency and H as the ocean depth) to conserve potential vorticity, making topography an important player in steering the mean path of the ACC. In particular, large topographic features reduce the temporal variability of the major front locations (Sallée et al. 2008), locking ocean jets "into place" (Sokolov and Rintoul 2009). These features are generally associated with downstream regions of enhanced surface eddy activity (Naveira Garabato et al. 2011) and increased cross-stream transport of tracers (Lu and Speer 2010; Sallée et al. 2011; Thompson and Sallée 2012; Abernathey and Cessi 2014), suggesting that topographic features play a role in setting the location and magnitude of eddy effects.

Most studies of jet–eddy–topography interactions focus on depth-integrated eddy kinetic energy (EKE) or rely on measurements of surface velocity obtained from altimetry (e.g., Meredith and Hogg 2006). However, neither the Southern Ocean flow nor its eddy field is uniform with depth. This depth dependence of the flow is a determining factor in the dynamical response of the ACC to changes in winds (Morrison and Hogg 2013; Langlais et al. 2015). Eddy activity at depth remains poorly characterized, yet has important implications for ocean dynamics.

Deep-reaching eddies that interact with rough topography can lead to significant energy dissipation through lee-wave generation (Nikurashin et al. 2012), and field measurements have shown that eddy energy at depth is closely related to the local rates of turbulent mixing (Sheen et al. 2014). A current challenge in our attempts to better characterize abyssal dissipation and mixing is an incomplete understanding of the deep eddy field; it cannot be obtained from satellite altimetry but relies on in situ measurements (e.g., Firing et al. 2011; Waterman et al. 2013), which remain scarce and have limited temporal and spatial scope. Recent efforts to monitor the Drake Passage using moored instruments provided estimates of EKE at depth. For example, Sheen et al. (2014) report strong seasonal fluctuations in EKE at 3600 m (between 0 and $120\,\mathrm{cm^2\,s^{-2}}$ over a 2-yr period) from a mooring deployed on the mean path of the Subantarctic Front. Chereskin et al. (2009) provide an estimate of near-bottom EKE from an array of bottom-moored sensors in Drake Passage, showing strong spatial variations across the region between two ACC fronts, with 1-yr mean EKE varying between 50 and $200\,\mathrm{cm^2\,s^{-2}}$ (see their Fig. 3c). These advances in Southern Ocean monitoring are supplemented by modeling studies, which provide spatial and temporal information where observations are lacking. In particular, Thompson and Naveira Garabato (2014) investigate regions of topography-induced stationary meanders in the Southern Ocean and highlight the full-depth enhancement of EKE at these sites (their Figs. 4b and 6b), with peak values of EKE at 2500 m reaching $50–100\,\mathrm{cm^2\,s^{-2}}$.

The main goal of this study is to better understand what sets the spatial distribution and magnitude of deep EKE in regions where Southern Ocean jets interact with topographic features and sustain stationary meanders. We approach this complex question by investigating the interaction of an unstable jet with a single topographic feature, using a two-layer ocean model, similar to that of Hallberg and Gnanadesikan (2001). We focus on evaluating the impact of the presence, height, and shape of topography on the magnitude of the lower-layer EKE as

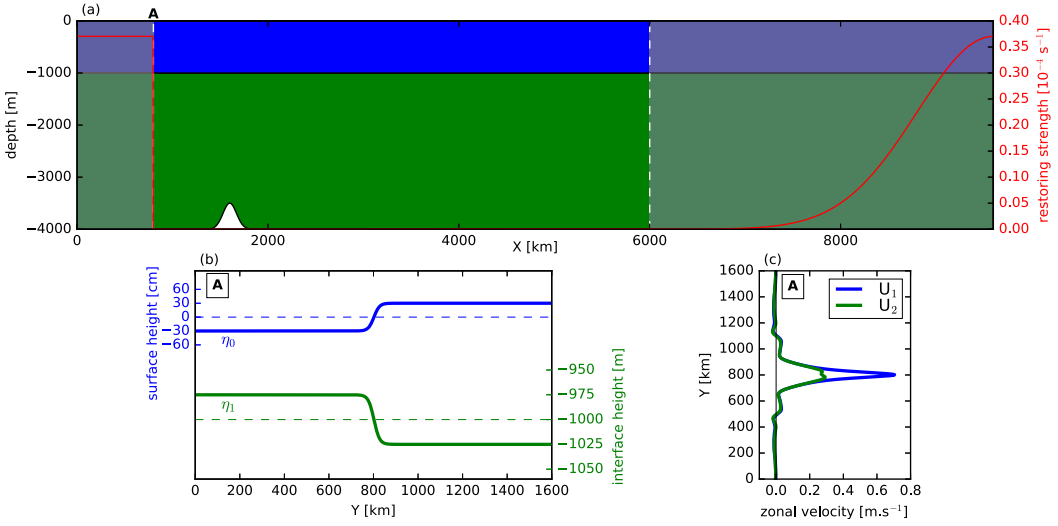

FIG. 1. (a) Elevation view of the domain at $y = 800$ km. The upper layer is shown in blue, and the lower layer is shown in green. A typical topography profile is visible in the lower layer. The restoring strength (red) is high in the forcing regions (shaded in gray). In the middle region, the flow evolves with no forcing. (b) Meridional profiles of the target heights for the free surface (blue) and the interface (green) at the inflow (section A, $x = 800$ km). The reference height of each interface is shown by a horizontal dashed line. (c) Meridional profile of the zonal velocity at the inflow (section A, $x = 800$ km) for our control experiment.

well as identifying the main pathways of energy conversion into the lower-layer EKE. The structure of the inflowing jet is an important factor in these complex interactions, and we investigate its impact by exploring a range of inflow conditions.

This paper proceeds as follows: In section 2, we present the details of the ocean model configuration and the energetic framework used to analyze the model output. In section 3, we first focus on the impact of topography on the vertical distribution of EKE and the relative contribution of two distinct energy pathways to deep EKE. We then investigate how these pathways to deep EKE respond to changes in the properties of the jet impinging on the topography. In section 4, we discuss the impact of topography and inflow conditions on EKE generation, examining the role of the topographic shape and the competing effects of inflow baroclinicity. Finally, in section 5, we summarize our findings and the implications for Southern Ocean circulation.

2. Methods

We perform our study using an idealized model of an isolated jet impinging on topography. The model uses the Modular Ocean Model, version 6 (MOM6; http://github.com/NOAA-GFDL/MOM6), to solve the hydrostatic thickness-weighted primitive equations under the Boussinesq approximation. The core of MOM6 is based on the Generalized Ocean Layer Dynamics (GOLD) ocean code, which is presented in detail in Adcroft and Hallberg (2006). It is configured using isopycnal coordinates, which eliminates the spurious diapycnal mixing produced by numerical ocean models that use a fixed vertical coordinate (Ilicak et al. 2012).

a. Model configuration

We model a representative section of the Southern Ocean by a $9600 \times 1600\,\text{km}^2$ channel on a β plane (with $\beta = 1.5 \times 10^{-11}\,\text{m}^{-1}\,\text{s}^{-1}$), with a horizontal resolution of 4 km and two isopycnal layers. These two layers have reference depths of $H_1 = 1000$ m and $H_2 = 3000$ m (Fig. 1a) to represent the intensification of the jet observed in the upper 1000 m of the ocean (e.g., Waterman et al. 2013). Although this vertical structure is a simplification of the continuously stratified ocean, using two layers provides an ocean model that supports both barotropic and baroclinic instabilities, with minimal computational overhead. Furthermore, the minimal complexity of the model allows a detailed analysis of energy transfers in the system and their sensitivity to topography and inflow properties. This study focuses on exploring the response of dynamical processes to topography, not on providing quantitative estimates of EKE in specific Southern Ocean locations, and the results should be interpreted with that aim in mind.

The model is discretized on an Arakawa C grid in the horizontal. A piecewise parabolic method (PPM) is used to solve for continuity. The advection scheme is enstrophy conserving (and energy conserving for nonhorizontally divergent flows). Time stepping is performed using a barotropic–baroclinic split, with time steps of 12 and 120 s,

respectively. The background horizontal viscosity is parameterized with a biharmonic horizontal viscosity of $A_4 = 1.5 \times 10^9\,\mathrm{m^4\,s^{-1}}$. This small value of viscosity allows numerical stability, while ensuring we represent a relatively inviscid ocean interior. Bottom friction is modeled by a weak quadratic bottom drag (with $C_{\mathrm{drag}} = 5 \times 10^{-4}$). No diabatic effects are included in the interior of the channel (in particular, there is no buoyancy forcing or diapycnal mixing).

b. Forcing and boundary conditions

The forcing and boundary conditions are chosen to sustain an eastward-flowing jet, representative of a typical Southern Ocean frontal jet. The boundary conditions are free slip at the southern ($y = 0$ km) and northern ($y = 1600$ km) boundaries, while the eastern and western boundaries are periodic. These numerical boundary conditions are supplemented by regions of numerical forcing (referred to as sponges; gray shading in Fig. 1a) at specified boundary regions in the channel to drive the flow in the interior. In the western part of the domain ($0 < x < 800$ km), we generate a sharp front and a jet flowing eastward through the basin by restoring both the interface and free-surface heights to target profiles (Fig. 1b). The target profiles are hyperbolic tangent functions centered on reference heights ($\eta_0 = 0$ for the free surface and $\eta_1 = -1000$ m for the interface), with a width of $\Delta y = 25$ km and maximum amplitudes of $\pm\Delta\eta_0$ and $\pm\Delta\eta_1$ (which vary between runs). The values of $\Delta\eta_0$ and $\Delta\eta_1$ are chosen to produce an inflowing velocity profile relevant to observed Southern Ocean jets (see section 2c). We use a short (45 min) restoring time scale to precisely control the flow in this forcing region. The circulation in the interior is not significantly affected by a change in this forcing time scale, provided it is short enough to effectively constrain the inflow. This setup ensures that we can study the dynamics of the jet in the interior ($x > 800$ km) while constraining the inflowing jet properties. On the eastern side of the domain ($6000 < x < 9600$ km), we introduce an additional restoring to allow a gradual readjustment of the outflow to match the inflow condition imposed at the western boundary.

Interface heights are weakly restored at the northern and southern boundaries to maintain a large-scale meridional isopycnal slope across the channel. This restoring toward our target heights ($\pm\Delta\eta_0$ and $\pm\Delta\eta_1$) is applied in 100-km-wide regions along the northern and southern boundaries of the channel, with a slow restoring time scale of 20 days.

c. Experimental design

The circulation in the interior of the model domain is forced with a range of inflow conditions and two types of bottom topography. Both the topography characteristics and the inflow conditions are described in detail below.

For simplicity, we introduce a single topographic feature in the lower layer. Two distinct types of topography are used: the first is an axisymmetric seamount and the second is a ridge, which spans the domain in the meridional direction. The zonal profile used for both topography types is Gaussian in shape, with a half-width $L_{\mathrm{topo}} \approx 150$ km and a maximum elevation of $h_{\mathrm{topo}} = 50, 150,$ or 500 m. The topography is placed 800 km from the downstream edge of the inflow sponge region ($x_0 = 1600$ km) and aligned with the inflowing jet ($y_0 = 800$ km). The horizontal scale of the seamount is large compared to the width of the jet and represents broad topographic plateaus, such as the Kerguelen and Campbell Plateaus, while the meridional ridge can be thought of as an idealized Macquarie Ridge. The range of heights considered explores the transition between a flat bottom and a single piece of topography as well as the sensitivity to a change in topography height. The range was limited to values below 500 m due to the high impact of the topography on the upper-layer flow for heights beyond 500 m in this two-layer system.

In our control experiment, the forcing parameters are set to default values of $\Delta\eta_0 = 30$ cm and $\Delta\eta_1 = 25$ m in the western sponge region. These values are chosen to approximate the typical velocity, width, and depth profile of Southern Ocean frontal jets, as observed during the recent Southern Ocean Finestructure (SOFINE; http://archive.noc.ac.uk/SOFINE) and DIMES (http://dimes.ucsd.edu) projects. These jets have typical meridional widths of 50–150 km and peak velocities of 0.5–$1\,\mathrm{m\,s^{-1}}$ (in the upper 500–1000 m), while velocity below 1000 m is of order $0.1\,\mathrm{m\,s^{-1}}$ (Waterman et al. 2013; Sheen et al. 2014). In our model, the prescribed default values of $\Delta\eta_0$ and $\Delta\eta_1$ generate the jet velocity profile at the inflow presented in Fig. 1c, with a meridional width of $O(100)$ km in both layers and peak velocities of $0.8\,\mathrm{m\,s^{-1}}$ in the upper layer (blue) and $0.3\,\mathrm{m\,s^{-1}}$ in the lower layer (green). The horizontal and vertical shear in the velocity fields at the inflow implies that the jet has potential for both barotropic and baroclinic instabilities [following Pedlosky's (1963) necessary conditions for instabilities]. We vary the large-scale meridional height differences, $\Delta\eta_0$ and $\Delta\eta_1$, in a series of parameter study runs. The surface height difference $\Delta\eta_0$ ranges between 15 and 45 cm, and the interface height difference $\Delta\eta_1$ ranges between a fully barotropic forcing ($\Delta\eta_1 = 0$) and a strongly baroclinic forcing ($\Delta\eta_1 = 37.5$ m). The range of forcing parameters considered in this study is summarized in Table 1.

Each simulation is started from rest (where both interfaces are flat) and run until the model reaches a statistically steady state (approximately 10 model years). We assess whether the run is in statistical equilibrium

TABLE 1. List of simulations performed and the associated parameter values.

	Inflow		Topography	
Run	$\Delta\eta_0$ (cm)	$\Delta\eta_1$ (m)	h_{topo} (m)	Shape
1	30	25	0	Flat
2	30	25	50	Seamount
3	30	25	500	Seamount
4	30	0	0	Flat
5	30	0	50	Seamount
6	30	0	500	Seamount
7	30	12.5	0	Flat
8	30	12.5	50	Seamount
9	30	12.5	500	Seamount
10	30	37.5	0	Flat
11	30	37.5	50	Seamount
12	30	37.5	500	Seamount
13	15	25	0	Flat
14	15	25	50	Seamount
15	15	25	500	Seamount
16	45	25	0	Flat
17	45	25	50	Seamount
18	45	25	500	Seamount
19	30	12.5	50	
20	30	12.5	150	
21	30	12.5	500	
22	30	25	50	
23	30	25	150	Ridge
24	30	25	500	
25	30	37.5	50	
26	30	37.5	150	
28	30	37.5	500	

using the time evolution of the total energy in the domain. Once the total energy is stable, the simulation is run for 3-yr periods, during which statistics are accumulated. This 3-yr period is long compared with the lifetime of an individual eddy, so results are not dominated by a single transient feature but by the long-term statistics of the flow.

d. Energetic framework

To quantify the change in the EKE in the lower layer of our isopycnal model, we use a thickness-weighted energy framework similar to that used by Bleck (1985) and Aiki et al. (2016), extended to include free-surface motions. This approach allows us to quantify how the time-mean and eddy energy reservoirs and the local energy conversions between these reservoirs depend on the characteristics of the inflowing jet and the topography it encounters.

1) ENERGY RESERVOIRS

Our two-layer system has four main energy reservoirs, defined as follows. The APE_{bt} reservoir is the available potential energy due to the free-surface elevation η_0 (or barotropic potential energy):

$$\text{APE}_{\text{bt}} = \frac{\rho_0}{2} g \eta_0^2. \tag{1}$$

The available potential energy due to the motions of the interface separating the upper and lower layers η_1 is APE_{bc} (or baroclinic potential energy):

$$\text{APE}_{\text{bc}} = \frac{\rho_0}{2} g' \eta_1^2. \tag{2}$$

The kinetic energy in each layer is KE_i ($i = 1, 2$):

$$\text{KE}_i = \frac{\rho_0}{2} h_i |\mathbf{u}_i|^2, \quad (\text{for } i = 1, 2). \tag{3}$$

Here, ρ_0 is the reference density of the Boussinesq approximation, g is the acceleration due to gravity, $g' = (g\Delta\rho)/\rho_0$ is the reduced gravity of the interface between the two layers, h_i is the ith layer thickness, and $\mathbf{u}_i = (u_i, v_i)$ is the horizontal velocity in layer i.

2) MEAN-EDDY DECOMPOSITION

To separate the mean and eddy terms, we define the traditional Reynolds decomposition for most variables in our model. For example, the layer thickness becomes

$$h_i \equiv \overline{h_i} + h_i', \tag{4}$$

where the overbar and prime symbols denote a 3-yr time mean and the associated deviation, respectively. Following the methodology used in Aiki et al. (2016), the velocity variable is decomposed into a thickness-weighted mean (TWM) velocity $\hat{\mathbf{u}}$ and deviation from the TWM mean $\mathbf{u}_i''$:

$$\mathbf{u}_i \equiv \hat{\mathbf{u}}_i + \mathbf{u}_i''. \tag{5}$$

In a thickness-weighted framework, each energy reservoir can be decomposed into contributions from the mean and eddy, as proposed by Bleck (1985):

$$\overline{\text{APE}_{\text{bt}}} = \overline{\frac{\rho_0}{2} g \eta_0^2} = \underbrace{\frac{\rho_0}{2} g \overline{\eta_0}^2}_{\text{MAPE}_{\text{bt}}} + \underbrace{\frac{\rho_0}{2} g \overline{\eta_0'^2}}_{\text{EAPE}_{\text{bt}}}, \tag{6}$$

$$\overline{\text{APE}_{\text{bc}}} = \overline{\frac{\rho_0}{2} g' \eta_1^2} = \underbrace{\frac{\rho_0}{2} g' \overline{\eta_1}^2}_{\text{MAPE}_{\text{bc}}} + \underbrace{\frac{\rho_0}{2} g' \overline{\eta_1'^2}}_{\text{EAPE}_{\text{bc}}}, \quad \text{and} \tag{7}$$

$$\overline{\text{KE}_i} = \overline{\frac{\rho_0}{2} h_i |\mathbf{u}_i|^2} = \underbrace{\frac{\rho_0}{2} \overline{h_i} |\hat{\mathbf{u}}_i|^2}_{\text{MKE}_i} + \underbrace{\frac{\rho_0}{2} \overline{h_i |\mathbf{u}_i''|^2}}_{\text{EKE}_i}, \quad (\text{for } i = 1, 2). \tag{8}$$

Note that the kinetic energy is decomposed using the TWM decomposition of velocity. Also, this eddy-mean decomposition is based on the separation between

stationary (i.e., mean) and transient (i.e., eddy) features. Thus, the contribution of stationary meanders, or stationary eddies, are included in the contribution of the time-mean flow.

3) Local sources of eddy kinetic energy

The equations that govern the time evolution of the six energy reservoirs defined in (6)–(8) can be derived from the incompressible hydrostatic equations of motion in isopycnal coordinates (see the appendix for the derivation of all energy reservoirs). In particular, the time evolution of the eddy kinetic energy EKE_i is governed by the following equation:

$$\begin{aligned}\partial_t \mathrm{EKE}_i = &-\nabla\cdot(\hat{\mathbf{u}}_i \mathrm{EKE}_i) - \nabla\cdot(\overline{\mathbf{u}_i'' \mathrm{EKE}_i}) \\ &- \overline{\mathbf{u}_i''\cdot h_i \nabla\phi_i'} + \rho_0 \hat{\mathbf{u}}_i\cdot\nabla\cdot\overline{(h_i \mathbf{u}_i''\otimes\mathbf{u}_i'')} \\ &+ \rho_0 \overline{h_i \boldsymbol{F}_{\tau i}\cdot\mathbf{u}_i''}, \quad (\text{for } i=1,2), \end{aligned} \tag{9}$$

where $\otimes$ denotes the outer product of two vectors. Here, $\phi_1 = \rho_0 g\eta_0$ and $\phi_2 = \phi_1 + \rho_0 g'\eta_1$ are the Montgomery potential anomalies in the upper and lower layer, respectively, and $\mathbf{F}_{\tau i}$ is the frictional force (including both interior viscosity and bottom drag) at work in each layer. Note that the thickness-weighted energy framework leads to a decomposition of the energy reservoirs and energy fluxes that differs from the commonly used approach of Lorenz (1955) and has the advantage of explicitly representing the energy flux due to layer thickness form stress.

The right-hand side of (9) can be interpreted as transfers of energy in and out of the eddy kinetic energy reservoir. These energy transfers include advective terms, expressed as a flux divergence, and local conversion terms. In this study, we focus only on the terms that locally convert energy into the deep eddy kinetic energy reservoir EKE_2, summarized in Fig. 2. Therefore, the first two terms on the right-hand side of (9), which are advective in nature and represent nonlocal interactions (e.g., Chen et al. 2014), are not included in our analysis. The remaining terms are as follows:

- The term $\rho_0\hat{\mathbf{u}}_2\cdot\nabla\cdot\overline{(h_2\mathbf{u}_2''\otimes\mathbf{u}_2'')}$ represents the work of Reynolds stresses within the lower layer (green line in Fig. 2). This is a bidirectional term between the mean and eddy kinetic energy reservoirs in the lower layer. It is positive when mean energy is converted into eddy energy through horizontal shear instabilities within the layer and negative when eddy momentum fluxes act to strengthen the mean flow (i.e., net flux from eddy energy into mean energy).
- The term $-\overline{\mathbf{u}_2''\cdot h_2\nabla\phi_2'}$ represents the work of eddy form stress for the lower layer (orange line in Fig. 2). It arises due to correlations between the eddy velocities and horizontal pressure differences at the undulating interior interface. This is a bidirectional term that can convert energy into or out of EKE_2. This energy is sourced either through conversion from eddy available potential energy (EAPE) via interface motions or from mean kinetic energy (MKE) through the work of form stress, as shown by the blue dot marking the 3-way junction in Fig. 2. This term is defined as positive when it is a source of EKE and negative when it is a sink.
- The term $\rho_0\overline{h_2\mathbf{F}_{\tau 2}\cdot\mathbf{u}_2''}$ represents the dissipation in the lower layer from interior viscosity and bottom drag. In the absence of wind forcing, the work of frictional forces is dissipative and will act as a local sink of eddy kinetic energy.

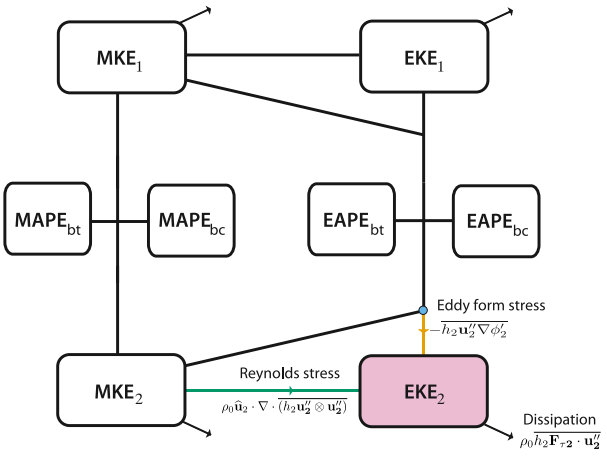

FIG. 2. Simplified energy diagram of our two-layer ocean based on energy equations presented above. Each energy reservoir is decomposed into mean and eddy contributions. The lines represent local conversion terms that flux energy between the reservoirs. Our study focuses on examining the lower-layer EKE and the conversions to this reservoir via eddy form stress, Reynolds stress, and dissipation (highlighted in color).

The relative magnitude, spatial patterns, and changes of these conversion terms are used in the following sections to understand the processes and energy pathways responsible for changes in lower-layer EKE.

3. Results

a. Isolated seamount

1) Instantaneous and time-mean jet structure

The inflowing jet for the flat-bottom control case is unstable and develops finite-amplitude meanders (Figs. 3a,d). In this case, the time-mean jet remains zonal (black contours in Figs. 3a,d), but the sharp jet forced at

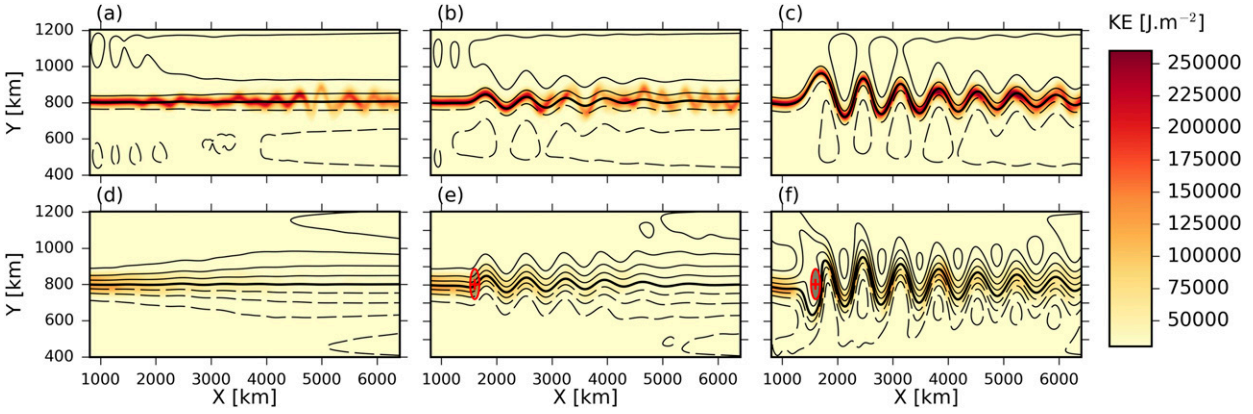

FIG. 3. The 5-day average of total KE (J m^{-2}; color) and 3-yr average transport [contours: 20-Sv (1 Sv $\equiv 10^6$ m^3 s^{-1}) streamlines] in the (top) upper and (bottom) lower layers for the (a),(d) flat-bottom case, the (b),(e) case with a seamount of $h_{\text{topo}} = 50$ m, and the (c),(f) case with a seamount of $h_{\text{topo}} = 500$ m. The inflowing jet used in each run is the control case ($\Delta\eta_0 = 30$ cm; $\Delta\eta_1 = 25$ m). The 3-yr mean jet axis is marked by the thick contour. The seamount location is shown in red (cross = center; circle = half height).

the western boundary broadens and weakens downstream. The addition of an isolated seamount alters the circulation by perturbing the jet in the vicinity of topography (Figs. 3b,c,e,f). With an isolated seamount of maximum height $h_{\text{topo}} = 50$ m, the jet develops vertically coherent, stationary meanders downstream of topography, visible in both the instantaneous kinetic energy and time-mean streamlines in each layer (Figs. 3b,e). When the seamount is high ($h_{\text{topo}} = 500$ m), the stationary meanders increase in meridional amplitude (Figs. 3c,f). The region of sustained stationary meanders also extends zonally to fill the length of the region of study.

2) EDDY KINETIC ENERGY

The presence of a seamount affects both the horizontal and vertical distribution of EKE. In the flat-bottom case, the onset of finite-amplitude instabilities at $x \approx 2500$ km results in an EKE increase broadly distributed in the horizontal and concentrated in the upper layer (colors in Figs. 4a,d). The seamount cases differ in both upper- and lower-layer EKE. In these cases, the high values of upper-layer EKE are constrained to the core of the meandering jet, especially in the high seamount case (Fig. 4c). On the other hand, in the lower layer the EKE increases and is spread more broadly (Fig. 4f). The range of EKE values in the lower layer remains an order of magnitude smaller than in the upper layer, but the basin-integrated, lower-layer EKE reaches 73% of the upper-layer EKE in the high seamount case.

The change in EKE due to topography is highlighted by showing the zonal dependence of meridionally averaged EKE (Fig. 5). In the flat-bottom case, the EKE in each layer increases slowly with downstream distance, reaching a maximum around $x \approx 3500$ km. It then decays with distance downstream (solid line). When a small seamount is present ($h_{\text{topo}} = 50$ m; dotted line), the upper-layer EKE maximum shifts farther downstream (by about 500 km), and its magnitude is reduced

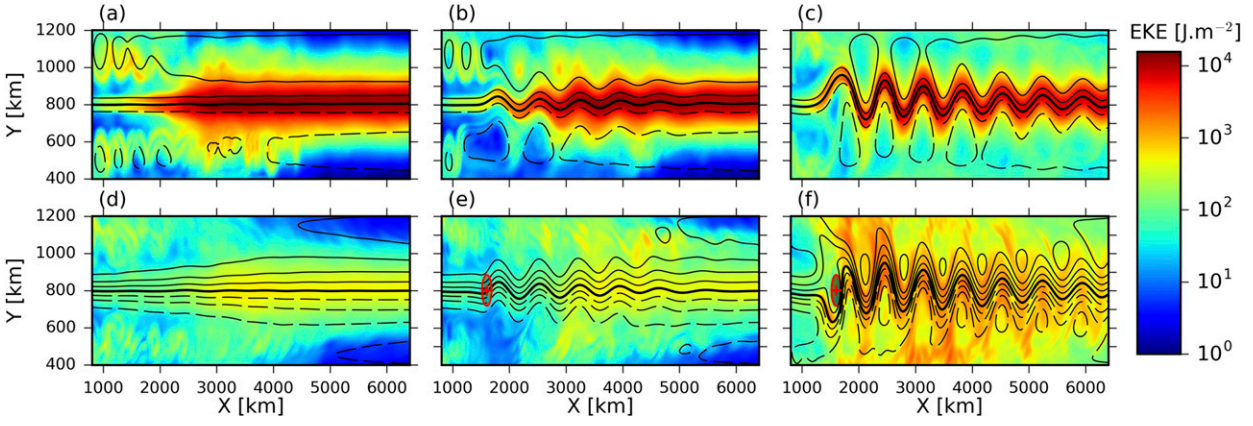

FIG. 4. As in Fig. 3, but for the 3-yr average of eddy kinetic energy (J m^{-2}; color) and time-mean transport (contours: 20-Sv streamlines).

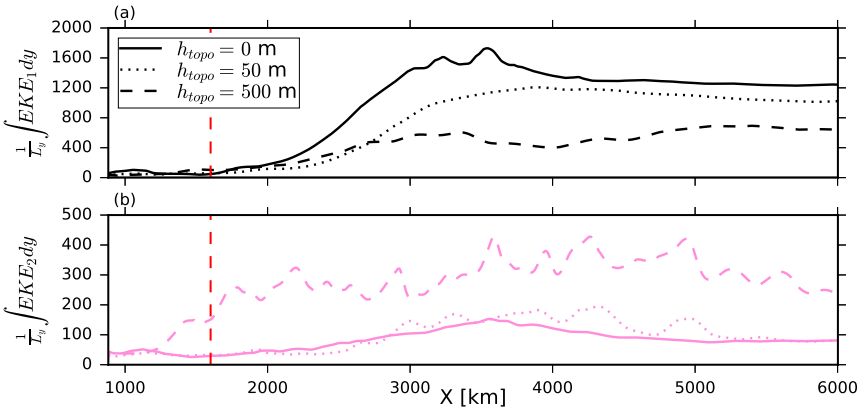

FIG. 5. Eddy kinetic energy (J m^{-2}) in the (a) upper layer and (b) lower layer, averaged over the basin width, for a seamount of height h_{topo} = 0, 50, and 500 m. The control inflow forcing ($\Delta\eta_0$ = 30 cm; $\Delta\eta_1$ = 25 m) is used for the three runs. The seamount location is marked by the red dashed line.

everywhere compared with the flat-bottom case. The lower-layer EKE shows a similar downstream shift, but its magnitude is marginally larger than the flat-bottom case. When the seamount is high (h_{topo} = 500 m; dashed line), the upper-layer EKE is further reduced (to about half of the flat-bottom values), while the peak values of the lower-layer EKE are tripled compared to the flat-bottom simulation. In this case, the zonal evolution of the lower-layer EKE shows signatures of the stationary meanders downstream of the seamount as well as enhanced eddy activity upstream of the location of the seamount peak ($x \leq 1600$ km).

These three cases have a similar basin-integrated total mechanical energy (data not shown) but show significant differences in the vertical partitioning of their eddy kinetic energy, despite being forced with the same inflowing jet. In the flat-bottom case, EKE is concentrated in the upper layer, while in the presence of a seamount, the upper-layer EKE decreases in magnitude and the lower-layer EKE is enhanced. The repartition of upper and lower EKE becomes more extreme as the height of the topography is increased, resulting in EKE values of the same order of magnitude across both layers in a 500-m seamount case.

3) ENERGY CONVERSION PATHWAYS

Variations in the magnitude of EKE induced by the presence of topography suggest that the rate of energy conversion to EKE from other energy reservoirs has changed. To understand how the energy fluxes to the lower-layer EKE are affected by topography, we examine the x-integrated work of lower-layer Reynolds stress (green line in Figs. 2 and 6a) and eddy form stress (orange line in Figs. 2 and 6b) for a seamount with heights h_{topo} = 0, 50, and 500 m.

In the flat-bottom case (solid line), we find that the work of Reynolds stress is positive in the upstream part of the basin (until $x \approx 3000$ km) and is negative

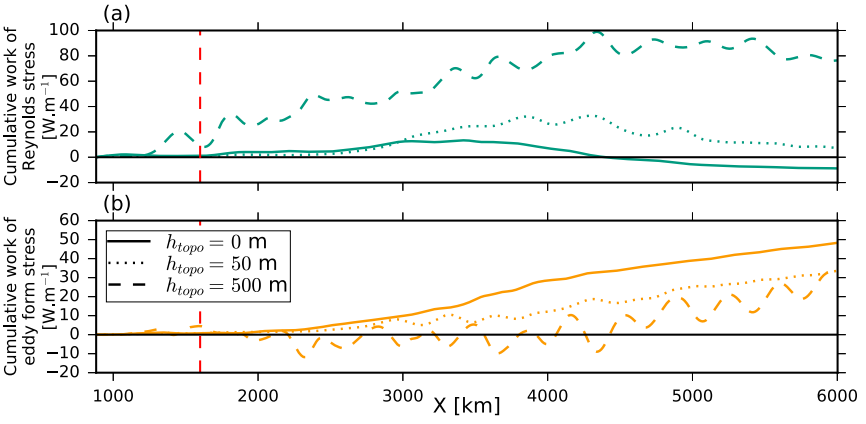

FIG. 6. As in Fig. 5, but for the cumulative sum of meridionally averaged work (W m^{-1}) of (a) Reynolds stress and (b) eddy form stress in the lower layer.

downstream ($x \gtrsim 3000$ km). When integrated over the length of the basin, the net work of Reynolds stress is negative, thus removing eddy energy (Fig. 6a). In contrast, the work of eddy form stress in the flat-bottom case is uniformly positive and contributes to a net conversion of energy into lower-layer EKE of 50 W m^{-1} (Fig. 6b). Thus, the net source of energy for lower-layer EKE in this case is the eddy form stress. Reynolds stress varies zonally but causes a net reduction in EKE (accounting for a zonally integrated flux of -10 W m^{-1}).

The zonal variations in the Reynolds stress term help to interpret the zonal evolution of variations in the lower-layer EKE (Fig. 5b). The increase in EKE in the upstream section of the basin can be attributed to energy conversion from the mean flow to the eddy field through the combined work of Reynolds and eddy form stresses, indicated by a collocated decrease in mean kinetic energy (not shown) and the positive work of Reynolds stresses integrated over this region (solid line in Fig. 6a). Farther downstream, eddy form stress continues to supply deep EKE, while Reynolds stress extracts energy from the eddies so that EKE slowly decays with downstream distance.

When a small seamount is present, the total contribution of Reynolds stress increases, adding up to a net positive flux within the basin (dotted line in Fig. 6a). The cumulative work of Reynolds stress shows a similar zonal variation to the flat-bottom case, but the peak shifts downstream by about 1000 km (similar to the downstream shift in the EKE peak; Fig. 5b). The eddy form stress contribution is positive everywhere, but 30% smaller than its basin-integrated contribution in the flat-bottom case (dotted line in Fig. 6b). Overall, the net contribution from eddy form stress remains approximately 3 times larger than from the Reynolds stress.

When the seamount is high, the work of Reynolds stress is further increased (dashed line in Fig. 6a). The zonal variations in Reynolds stress are less pronounced: the local contributions of Reynolds stress accumulate steadily until $x = 4300$ km, after which the cumulative contribution plateaus. Notable differences in the zonal variations of Reynolds stress work in the high seamount case compared with the no and low topography cases include a positive energy flux upstream of the seamount and an extended region of steady increase (which covers most of the domain). The basin-integrated contribution of Reynolds stress remains positive, totaling 80 W m^{-1}, far above that of the flat and small seamount cases (which reach about -10 and 10 W m^{-1}, respectively). On the other hand, the eddy form stress is further reduced when the seamount is high (dashed line in Fig. 6b). Its cumulative contribution is negligible for $x < 4000$ km, after which it increases steadily, albeit modulated by stationary meanders. The basin-integrated contribution of eddy form stress is similar to the small seamount case (32 W m^{-1}).

Thus, when the jet interacts with a high seamount, the local conversion of energy into lower-layer EKE is mostly done through the work of lower-layer Reynolds stress, with a smaller contribution from eddy form stress. This balance differs from the small seamount and flat-bottom cases, where eddy form stress is the main contributor to the deep EKE reservoir. This shift in the relative importance of the two energy conversion terms is mostly due to an increased work by Reynolds stress in the basin, combined with a moderate reduction in the work of eddy form stress. As a result, the combined source of deep EKE is significantly larger when a high seamount is present, leading to an elevated deep EKE.

4) SENSITIVITY TO INFLOW

We now examine the sensitivity of the magnitude and sources of deep EKE to changes in the inflow conditions for the flat-bottom case and for the high seamount case. The inflow conditions can be characterized by 1) the depth-integrated transport, which is related to the total kinetic energy at the inflow, and 2) the partition of energy between the barotropic and baroclinic modes at the inflow, which we measure by a nondimensional baroclinicity index. This baroclinicity index is calculated as the ratio of interface APE to surface APE of the inflowing jet, denoted $(\mathrm{APE_{bc}}/\mathrm{APE_{bt}})|_{\mathrm{inflow}}$. In this study, we vary the baroclinicity index from 0 (fully barotropic inflow with no vertical shear) to 240 (strongly baroclinic, with a small depth-integrated transport).

We first consider the effect of these variations on deep EKE, in particular on the fraction of total mechanical energy (ME) contained in the deep EKE reservoir (Figs. 7a–c). Normalizing deep EKE by ME allows us to compare the relative importance of deep EKE across simulations that have different energy inputs at the inflow. Two important points are revealed by Figs. 7a–c. First, the presence of a seamount systematically increases the fraction of ME contained in deep EKE, relative to a flat-bottom case. The magnitude of this increase in deep EKE is higher for higher seamounts, consistent with the results presented in section 3a(2) for our control inflow, and higher in cases with more baroclinic inflows. One exception is the case of a strongly baroclinic inflow $[(\mathrm{APE_{bc}}/\mathrm{APE_{bt}})|_{\mathrm{inflow}} = 240]$ with a small, depth-integrated transport (dark blue; Fig. 7a), where the presence of a seamount has little effect on deep EKE, regardless of the seamount height. In this case, the lower-layer flow generated at the western boundary is weak ($u_{\max} < 0.05$ m s^{-1}), minimizing the impact of jet–topography interactions on the flow.

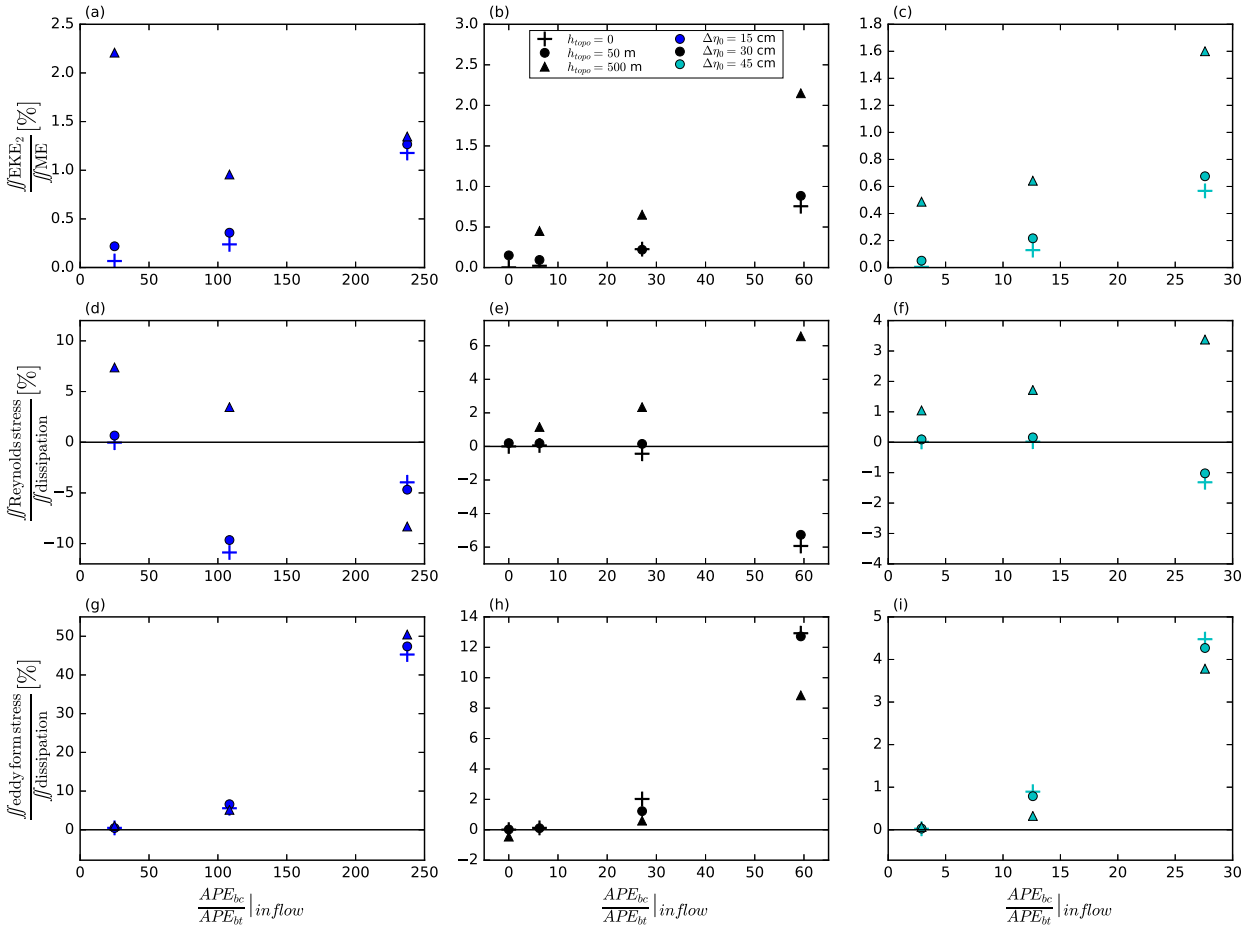

FIG. 7. Basin-integrated lower-layer (a)–(c) normalized eddy kinetic energy, (d)–(f) normalized work of the Reynolds stress, and (g)–(i) normalized work of the eddy form stress as a function of the inflow baroclinicity. The simulations include a range of seamount heights h_{topo} and inflow parameters $\Delta\eta_0$ and $\Delta\eta_1$. The lower-layer EKE is normalized by the basin-integrated total mechanical energy, while the energy fluxes are normalized by the basin-integrated energy dissipative flux. Positive values in (d)–(i) indicate a total flux of energy into the eddy kinetic energy reservoir. The case of a fully barotropic inflow interacting with a high seamount is outside the range shown on this figure.

The second point to note from Figs. 7a–c is that the normalized deep EKE increases with the baroclinicity of the inflow, whether a seamount is present or not. This response cannot be explained by the change in the incoming lower-layer mean flow (which is reduced with increased baroclinicity) and suggests a feedback between the baroclinicity of the inflow and the lower-layer eddy field, which will be examined using our energy analysis below. The exception to this response is the series of high seamount cases with low depth-integrated transport (dark blue triangles; Fig. 7a), where deep EKE can decrease with inflow baroclinicity.

An examination of the local energy conversion pathways allows us to investigate the dynamics of the deep EKE sensitivity to the inflow conditions. To compare the results across different inflows, the energy conversion terms are normalized by the basin-integrated energy dissipation. The response of the normalized work of Reynolds stress to changes in inflow baroclinicity (Figs. 7d–f) shows two main features. First, the presence of a high seamount ($h_{\mathrm{topo}} = 500$ m, triangles) generally leads to an increase in the work of Reynolds stress to convert deep mean kinetic energy into deep EKE, for most inflow conditions (Figs. 7e,f). Second, the presence of a high seamount changes the sensitivity of the work of Reynolds stress to inflow baroclinicity. In cases with a high seamount, an increase in inflow baroclinicity enhances the positive energy conversion through Reynolds stress (from mean kinetic energy to EKE), while in no or small seamount cases (plus signs and circles), this same increase leads to an increase in negative energy conversion through Reynolds stress (i.e., an increase in the sink of deep EKE). The response highlighted in Figs. 7e and 7f suggests that the increased baroclinicity of the

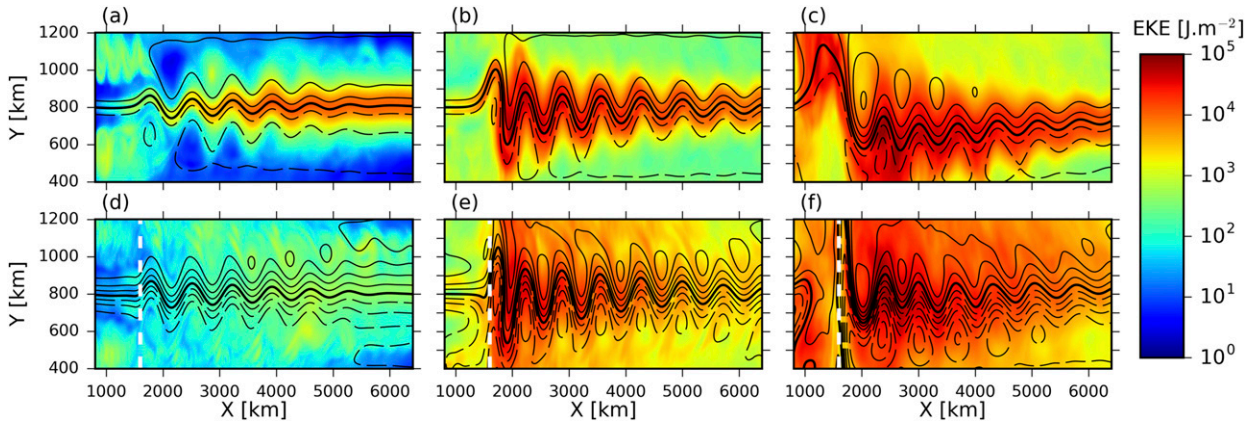

FIG. 8. Eddy kinetic energy (J m^{-2}; color) and time-mean transport (contours: 20-Sv streamlines) in the (top) upper and (bottom) lower layers for cases with a meridional ridge of (a),(d) h_{topo} = 50 m, (b),(e) h_{topo} = 150 m, and (c),(f) h_{topo} = 500 m. The inflowing jet used in all runs is the control case ($\Delta\eta_0$ = 30 cm; $\Delta\eta_1$ = 25 m). The jet axis is marked by the thick contour, and the ridge axis is marked by the white dashed line.

inflow enhances the eddy–mean flow interactions through the work of Reynolds stress, be it as a source or sink of EKE. The exceptions to the two points presented above are the cases with low depth-integrated transport (Fig. 7d), which show a decrease in normalized work of Reynolds stress with an increase in baroclinicity in the high seamount cases.

The response of the normalized work of eddy form stress to inflow baroclinicity (Figs. 7g–i) depends more strongly on the inflow characteristics than on the seamount height. The work of eddy form stress, whether a seamount is present or not, increases with inflow baroclinicity. The presence of a high seamount tends to reduce normalized eddy form stress in cases with more baroclinic inflows, as the increase in the total dissipation is higher than the increase in the net work of eddy form stress (not shown).

The changes in these two energy conversion pathways can help explain the behavior of the exceptional cases. In the case of a low depth-integrated transport, the small increase in deep EKE with inflow baroclinicity can be attributed to the interplay of the increase in eddy form stress with baroclinicity and a weaker contribution from Reynolds stress acting as a sink of deep EKE. Another special case is that of a fully barotropic inflow (not shown), where there is a significant increase in deep EKE in the case of a high seamount, which is primarily due to enhanced Reynolds stress work acting to convert mean energy into deep EKE, while the eddy form stress term is negligible. The increase in the work of Reynolds stress is consistent with both the strong lower-layer mean flow forced at the western boundary in this case and an increase in the energy of the eddy field due to the seamount, both leading to a total increase in eddy–mean flow interactions through Reynolds stress.

In summary, the work of eddy form stress is most sensitive to the baroclinicity of the inflow, irrespective of topography. However, with a high seamount (h_{topo} = 500 m), an increase in the baroclinicity index of the inflow also results in Reynolds stress work converting more deep mean kinetic energy into eddy energy. The magnitude of this deep EKE increase depends on the depth-integrated transport forced at the inflow, as shown by the higher sensitivity of both normalized conversion terms to baroclinicity in the larger transport cases (cyan) relative to the smaller transport cases (black; noting the different y axis scales).

b. *Interactions with a meridional ridge*

The lower-layer EKE generated by an unstable jet is not only strongly affected by the height, but also by the shape of the topography it encounters. This effect is demonstrated in our model using a meridional ridge, with the same zonal profile and zonal location as the seamount, extending across the entire basin width.

1) INSTANTANEOUS AND TIME-MEAN JET STRUCTURE

The presence of a ridge modifies the time-mean circulation and the spatial distribution of EKE in ways qualitatively similar to a seamount. The inflowing jet is deflected by the ridge, and stationary meanders are visible in the time-mean streamlines downstream in both the upper and lower layers (Fig. 8). The zonal wavelength of these stationary meanders is similar to that of the seamount cases (Fig. 4). The upper-layer EKE is enhanced in the jet core, while the lower-layer EKE is more broadly distributed horizontally. A small ridge (h_{topo} = 50 m; Figs. 8a,d) increases the lower-layer EKE compared with a flat-bottom case and is nearly indistinguishable

from a seamount of the same height (Figs. 4b,e). However, a higher ridge ($h_{\text{topo}} = 150$ m; Figs. 8b,e) enhances the lower-layer EKE more than a 500-m-high seamount (see Fig. 4f). Note that the lower-layer EKE is particularly strong in the first few meanders downstream of the ridge (Fig. 8e). A further increase in ridge height ($h_{\text{topo}} = 500$ m) increases the lower-layer EKE further (Fig. 8f). In this case, the ridge height leads to a partial blocking of the flow so that the downstream meanders in the lower-layer feed from a slope current coming from the forcing region at the northern boundary. Although previous studies have argued that a lower-layer flow from the boundary can be a realistic representation of Southern Ocean flows at depth (Hallberg and Gnanadesikan 2001), we prefer to present a ridge of intermediate height $h_{\text{topo}} = 150$ m as our "high ridge" case study, as the flow is more directly comparable with seamount cases where there is no blocking.

2) Eddy kinetic energy

When the jet encounters a meridional ridge, the deep EKE is enhanced, as in the case with a seamount. This relative enhancement of deep EKE is higher for higher ridges (cf. the diamonds to the plus signs in Fig. 9a), again similar to the seamount case. However, the proportion of energy contained in deep EKE is much higher for a meridional ridge that it is for a seamount (up to 14% of the basin-integrated energy compared with a maximum of 5% for seamount cases). Thus, the ridge is more effective in generating deep EKE than the seamount.

Figure 9a also shows that the sensitivity of deep EKE to inflow baroclinicity in the ridge case differs from that of the seamount case. For a small ridge ($h_{\text{topo}} = 50$ m), an increase in the baroclinicity of the inflow enhances the total lower-layer EKE (as in the flat case or the seamount cases). However, for a higher ridge ($h_{\text{topo}} = 150, 500$ m), an increase in the baroclinicity of the inflow reduces the total deep EKE. This behavior is opposite to that observed in the seamount cases. This distinct response suggests that the processes linking the inflowing jet to the interior flow are different in the seamount and ridge cases.

3) Energy conversion pathways

The work of lower-layer Reynolds stress (normalized by the total energy dissipation; Fig. 9b) is systematically larger in the presence of a ridge compared with the flat-bottom case, and its magnitude increases when the ridge increases in height. This response is qualitatively similar to the seamount cases, although the flux magnitude with a high ridge is 4–10 times higher than with a high seamount. When the inflowing jet is more baroclinic, the normalized work of Reynolds stress remains unchanged

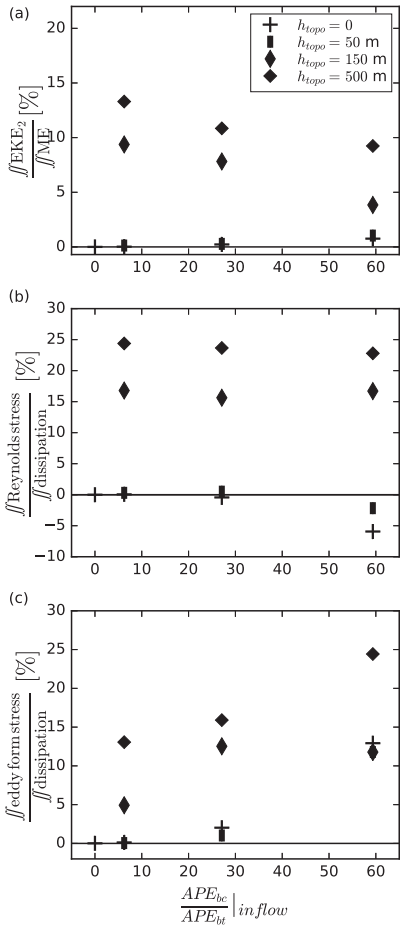

FIG. 9. As in Fig. 7, but for a meridional ridge of height $h_{\text{topo}} = 0$, 50, 150, and 500 m. The inflowing jet has a constant surface forcing of $\Delta\eta_0 = 30$ cm and an interface forcing $\Delta\eta_1 = 12.5$, 25, and 37.5 m. Note that the range on the y axis in (a) includes an additional order of magnitude compared with Fig. 7b.

for most ridge cases. This response differs from that observed in the corresponding cases with a seamount, where high topography cases show an increased work of Reynolds stress when the flow is strongly baroclinic (Fig. 7e).

The normalized work of eddy form stress on the lower layer is also much larger in the presence of a ridge compared with the flat-bottom case and increases with the height of the ridge (Fig. 9c). The normalized eddy form stress work in the ridge case is also systematically larger than in the corresponding seamount case (Fig. 7h), with a two- to tenfold increase in its contribution, depending on the inflow conditions. Its response to changes in the baroclinicity of the inflow is similar to the seamount cases, showing an increase in the work of eddy form stress when the flow is more baroclinic, although the intermediate ridge ($h_{\text{topo}} = 150$ m) shows no systematic trend.

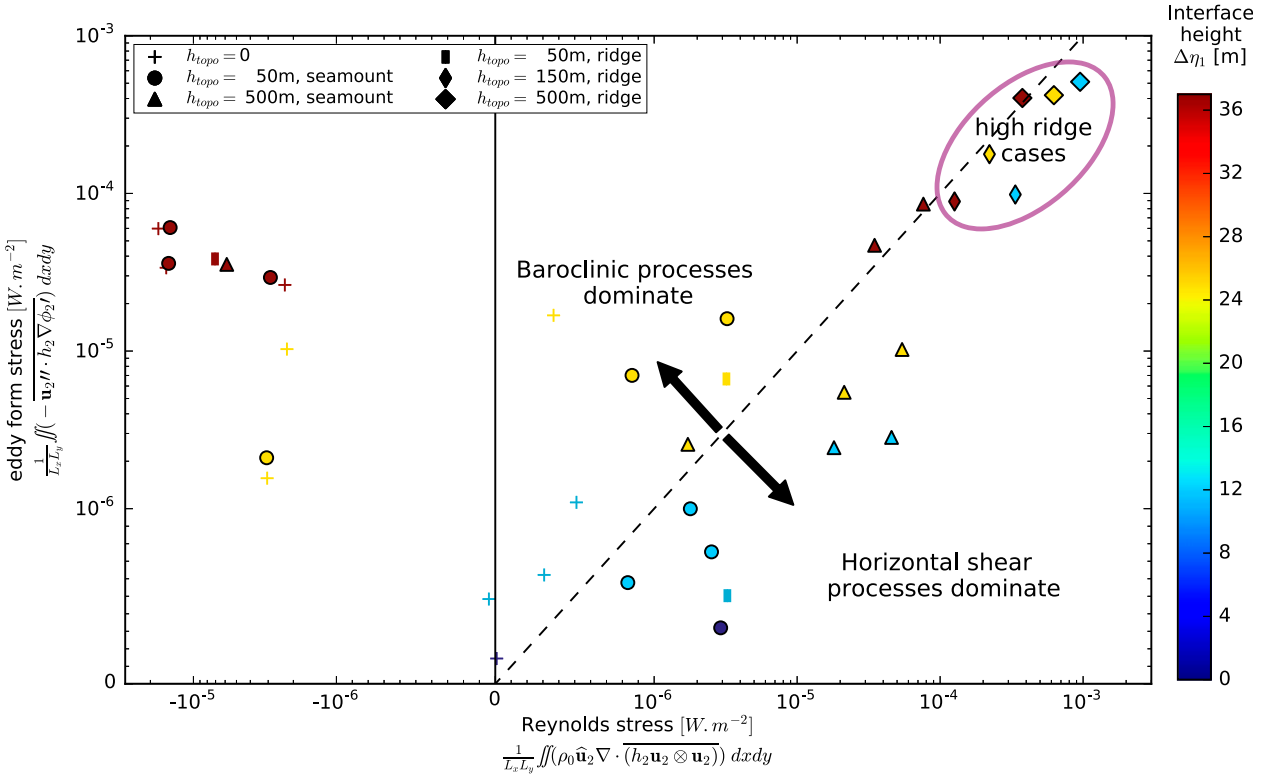

FIG. 10. Energy conversion to deep EKE through the work of Reynolds stress (x axis) and eddy form stress (y axis) for different topographies (symbols) and inflow interface slope (colors). A regime where both sources contribute equally would be located on the 1:1 line (dashed line). We consider cases above this line as dominated by baroclinic instability, while cases below this line are considered as dominated by horizontal shear instability. Simulations with a high ridge (◊ and ◇) are all located in the top-right corner. A cluster of simulations have negative Reynolds stress work (left-hand side of the plot), meaning that Reynolds stress acts as a sink of deep EKE, with baroclinic instability providing the source of deep EKE.

4. Discussion

The numerical experiments performed in this study provide evidence of the nature of the instability processes contributing to deep EKE, and how they depend on the structure of the topography and on the flow upstream of the obstacle.

a. Barotropic or baroclinic instability?

Comparing energy conversions to deep EKE through the two distinct pathways (Reynolds stress work versus work of eddy form stress) gives us insight into the relative contribution of different instability processes. All the simulations we consider are potentially unstable to mixed barotropic–baroclinic instabilities, due to the combination of horizontal and vertical shear in the jet profile [as is the case in the atmosphere, see Chang et al. (2002) and references within] Noting that a flow involving purely barotropic instability of the large-scale horizontal shear will generate EKE solely via the work of Reynolds stress and that purely baroclinic instability of the vertical shear generates EKE via the work of eddy form stress, we argue that in simulations where Reynolds stress is the dominant source of deep EKE, the flow is likely dominated by horizontal shear instability or, analogously, barotropic instability. Similarly, we consider simulations with large eddy form stress as systems dominated by baroclinic instability. In this way, the relative contribution of work by Reynolds stress and work by eddy form stress allows us to discriminate between different regimes, as summarized in Fig. 10.

Based on this framework, we observe that baroclinic instabilities are the dominant source of deep EKE for all simulations with a flat bottom (plus signs, located above the 1:1 broken line in Fig. 10), while Reynolds stress is either a small source or a sink of deep EKE. The relative contribution of these two energy pathways can be modified by either changing the inflowing jet structure or by introducing topography. Increasing the interface slope of the inflowing jet (colors in Fig. 10) predominantly increases the contribution from baroclinic instability to deep EKE (shift toward the top of Fig. 10). In contrast, the main effect of introducing a seamount of significant height is to increase the contribution from Reynolds stress (shift toward the right of Fig. 10). As a result, cases with a high seamount (triangles) have deep EKE predominantly sourced from deep horizontal

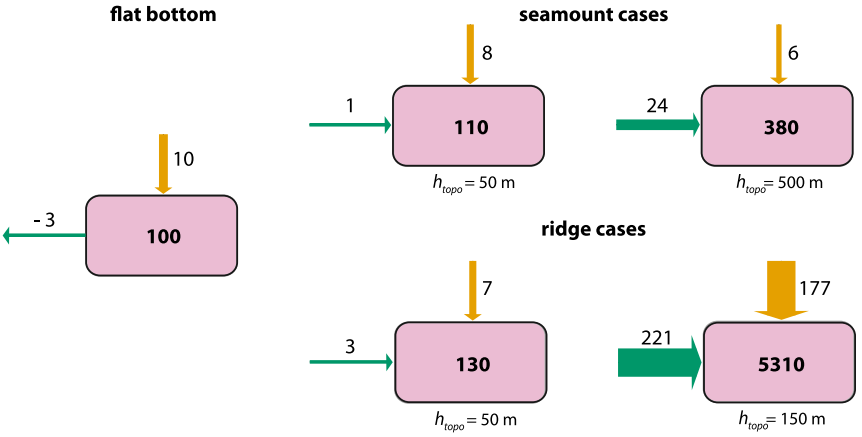

FIG. 11. Schematic energy diagram of lower-layer EKE for various cases of topography, showing the basin-averaged, lower-layer EKE (bold; J m^{-2}) and local conversions to lower-layer EKE (10^{-6} W m^{-2}) through the work of Reynolds stress (green horizontal arrow) and eddy form stress (orange vertical arrow). The flat-bottom case is shown on the left, and cases with topography (a seamount and a ridge respectively) are shown on the right. Here, the height of the seamount (50 m, 500 m) and ridge (50 m, 150 m) increase from left to right.

shear or have near-equal contribution from both sources (below, or close to, the 1:1 line on Fig. 10).

In contrast to the high seamount case, introducing a high ridge simultaneously increases both baroclinic and barotropic sources of deep EKE. All cases with a high ridge (narrow diamonds and wide diamonds in Fig. 10) sit close to the 1:1 line, indicating an equivalent contribution from both vertical and horizontal shear instabilities. The relative contribution of deep EKE sources is less sensitive to the inflowing jet structure than in cases with a seamount.

b. *Impact of topography*

Over the range of conditions explored in this study, all cases showed an increase in deep EKE in the presence of topography. This effect is summarized in Fig. 11, which compares the EKE_2 part of the energy diagram (bottom right-hand corner of Fig. 2) for various heights of topography. When we compare the seamount and the ridge cases, the differences in the magnitude of the deep EKE (bold numbers) and the relative contributions of deep EKE sources (green versus orange arrows) suggest that the effect of topography is twofold. First, the presence of topography deflects the jet along topographic height contours and generates meanders downstream. Within the meanders, the cross-jet velocity gradients are amplified, leading to horizontal shear, which generates eddies through the work of Reynolds stress (as exemplified by the seamount cases). In addition to this horizontal steering effect, the presence of topography enhances vertical shear over the top of the topography, which can contribute to deep EKE through the work of eddy form stress. This effect is most visible in the ridge case, which combines significant contributions from the work of both eddy form stress and Reynolds stress. The absence of this second effect in the seamount case is due to the ability of the jet to move around the seamount, effectively reducing the maximum topographic height experienced by the jet.

c. *Impact of inflowing jet structure*

We now consider the influence of the inflowing jet structure on the magnitude of deep EKE and the relative sizes of its sources (Fig. 12). An increase in the jet vertical shear leads to higher values of deep EKE in the flat-bottom and seamount cases (top and middle rows), while it leads to a decrease in the magnitude of deep EKE in the case of a high ridge (bottom row). The values in Fig. 12 are best used in reference to one another, keeping in mind that these net values (i.e., not normalized by the inflow conditions) are expected to change in magnitude across runs. The conflicting responses to a change in vertical shear can be reconciled by considering the two competing effects of an increase in vertical shear at the inflow. On the one hand, an inflow with a steep interface slope (strong vertical shear) is more likely to generate eddies through baroclinic instability. On the other hand, higher vertical shear implies a smaller velocity in the lower layer (for a given depth-integrated transport), which can reduce the jet–topography interactions. The first effect is dominant for the flat-bottom or seamount cases, where the work of eddy form stress is small and an increase in the vertical shear of the inflow provides increased potential for baroclinic instability to generate deep EKE. This result suggests that the eddy-generating potential of the baroclinic instability is a limiting factor and can be increased by a change in the inflow conditions. In contrast, the second effect is visible in the high ridge cases. Here, the magnitude of deep EKE and the work of eddy form stress are both large, and an

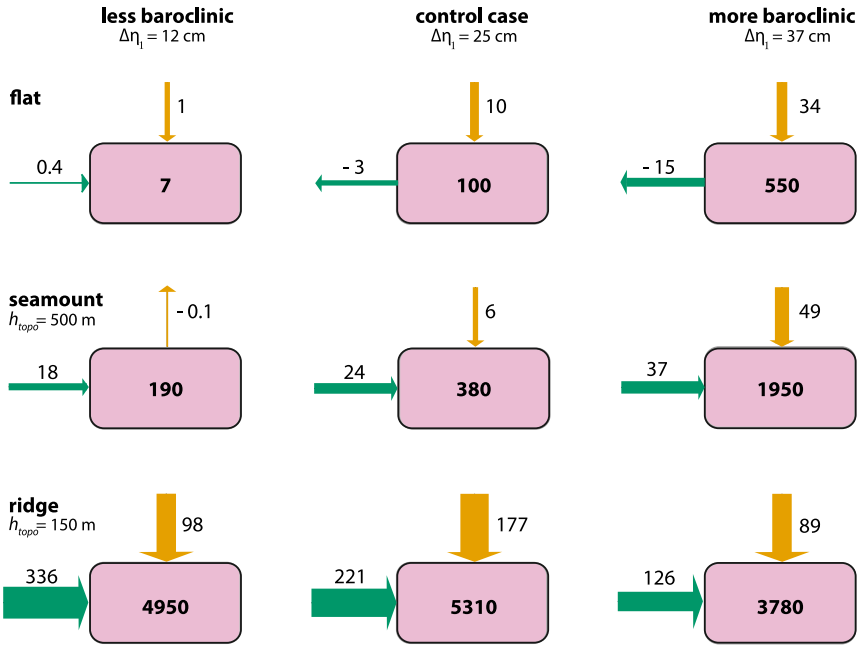

FIG. 12. Schematic energy diagram of lower-layer EKE for various cases of inflow vertical shear, showing the basin-averaged, lower-layer EKE (bold; $J\,m^{-2}$) and local conversions to lower-layer EKE ($10^{-6}\,W\,m^{-2}$) through the work of Reynolds stress (green horizontal arrow) and eddy form stress (orange vertical arrow). Three cases of topography are included, with (top) a flat bottom, (middle) a high seamount, and (bottom) a high ridge. The baroclinicity of the inflowing jet increases from left to right, with the control case in the center. All simulations shown here have the same surface forcing ($\Delta\eta_0 = 30$ cm).

increase in vertical shear reduces both the work of eddy form stress and the magnitude of deep EKE. This result suggests that in parameter regimes where baroclinic instability can fully develop, providing additional vertical shear upstream of topography does not provide additional EKE. Instead, the reduced topographic interaction due to a weaker lower-layer jet outweighs the added potential for baroclinic instability, thus reducing deep EKE overall.

Our experiments also tested the sensitivity of deep EKE to the free-surface slope. Although this parameter contributes to setting the absolute velocity at the inflow, the sensitivity of our results to this parameter was secondary compared with the role of the interface slope.

d. Caveats

Through the sensitivity experiments performed in this study, we find that the presence of topography modifies the partitioning of the total energy between different reservoirs and favors a relative increase in deep EKE. This enhancement of EKE downstream of topographic features is consistent with observations from field campaigns and previous modeling studies of the Southern Ocean (e.g., Hallberg and Gnanadesikan 2001; Thompson and Richards 2011; Thompson and Naveira Garabato 2014). The two-layer ocean model used has minimal complexity, yet it produces EKE values consistent with those observed in high-EKE regions of the Southern Ocean. For example, Sheen et al. (2014) reports values of EKE fluctuating between 0 and 80 $cm^2\,s^{-2}$ at 3600 m on the mean position of the Subantarctic Front in the Drake Passage, while Chereskin et al. (2009) report enhanced values of near-bottom EKE up to 200 $cm^2\,s^{-2}$. The results from the two-layer numerical experiments return peak values of lower-layer EKE within 1–300 $cm^2\,s^{-2}$, covering the range of observed, deep EKE values. While the simulations performed do not aim to reproduce the EKE at specific locations, the comparison with observed values increases our confidence in the relevance of the parameter space explored.

Relying on an idealized model results in some differences between the simulated and observed flow downstream of topography. One example of these is the zonal extent of the stationary meanders and the associated region of elevated EKE. In the simulations performed in this study, the meanders persist far downstream of topography (up to 3000–4000 km), while in observations and realistic ocean models (e.g., Thompson and Naveira Garabato 2014), they only extend over 100–1000 km, depending on the region considered. This difference in zonal extent is likely due to the idealized environment in the downstream region, where there are few disturbances to break down the meanders. We

note that such persistent meanders are visible in other idealized studies (e.g., Bischoff and Thompson 2014; Chapman et al. 2015). Furthermore, the full complexity of ACC dynamics cannot be investigated using this simple two-layer model, including the contribution that the merging of ACC jets (e.g., Lu and Speer 2010), the presence of higher-order baroclinic modes, or the local wind forcing can make to the spatial pattern of EKE.

5. Conclusions

Numerical simulations show a robust enhancement of deep EKE in the presence of topography, consistent with observations and previous studies. The height and shape of topography are both important in determining the magnitude and energy source of this EKE enhancement. Isolated obstacles allow the jet to avoid topographic features but produce narrow, meandering jets that generate deep EKE through horizontal shear instability. Broader topography, which cannot be avoided, additionally results in stronger vertical shear and baroclinic instability, increasing deep EKE by an order of magnitude. The height of the topographic feature is important in steering the jet path, but it is the height experienced by the flow along its mean path (e.g., gaps between features) that contributes to the baroclinic source of deep EKE.

This study also highlights the role of upstream conditions in determining the deep EKE magnitude and the sources of deep EKE. This sensitivity is largest when the jet is able to flow around the topography, as the upstream baroclinicity of the flow controls the baroclinic instability processes in the lee of topography. The upstream conditions are less influential when the jet–topography interactions alone lead to strong baroclinic instability.

We have focused on the impact of an isolated topographic feature. In the ocean, the topography is complex and has a variety of scales. The continuous changes in topography in the Southern Ocean mean it is unlikely for the downstream behavior to fully develop undisturbed by other topographic features, and the idealized shapes investigated in this study are simple limits to the behavior we expect from interactions with a more realistic topography. Nevertheless, these simulations serve to highlight that in the Southern Ocean, the EKE at depth is influenced by the topography characteristics and by the structure of the jet, which itself depends on the history of topographic interactions along its path. The resulting spatial heterogeneity in deep EKE will alter the spatial distribution of mixing and energy dissipation at depth.

Acknowledgments. The authors thank Aidan Heerdegen for his technical assistance in setting up the model as well as two anonymous reviewers who contributed to improve this manuscript. AB and AMH were supported by the Centre of Excellence for Climate System Science, Australian Research Council (AU) Grant CE1101028. AMH was also supported by an Australian Research Council Future Fellowship (FT120100842). SW gratefully acknowledges support from the Australian Research Council (DE120102927) and the National Science and Engineering Research Council of Canada (22R23085). SRK is supported by a UNSW Silverstar research grant. This research was undertaken on the NCI National Facility in Canberra, Australia, which is supported by the Australian Commonwealth Government.

APPENDIX

Derivation of Energy Budget in Two-Layer Framework

a. Time evolution of the total energy reservoirs

The equations that govern the time evolution of the four main energy reservoirs can be derived using their definitions [(1)–(3)] and the incompressible hydrostatic equations of motion in isopycnal coordinates [see Aiki et al. (2016), noting that we have extended their formulation to include $\mathrm{APE}_{\mathrm{bt}}$]. The resulting description of the time evolution of the reservoirs is

$$\partial_t \mathrm{APE}_{\mathrm{bt}} = \phi_1(\partial_t h_1 + \partial_t h_2), \tag{A1}$$

$$\partial_t \mathrm{APE}_{\mathrm{bc}} = (\phi_2 - \phi_1)\partial_t h_2, \quad \text{and} \tag{A2}$$

$$\partial_t \mathrm{KE}_i = -\nabla\cdot(\mathbf{u}_i \mathrm{KE}_i) - h_1 \mathbf{u}_i\cdot\nabla\phi_i + \rho_0 h_i \mathbf{F}_{\tau i}\cdot\mathbf{u}_i, \quad (\text{for } i = 1, 2). \tag{A3}$$

Here, $\phi_1 = \rho_0 g \eta_0$ and $\phi_2 = \phi_1 + \rho_0 g' \eta_1$ are the Montgomery potential (MP) anomalies in the upper and lower layer, respectively, and $\mathbf{F}_{\tau i}$ is the frictional force (including both interior viscosity and bottom drag) at work in each layer. The change in KE in each layer is driven by a combination of layerwise advective fluxes, the work of form stress and the energy dissipation through friction. The fluxes between the potential and kinetic energy are related through the MP flux divergence in each layer. The equation governing the MP flux divergence in the ith layer is

$$\nabla\cdot(\phi_i h_i \mathbf{u}_i) = -\phi_i \partial_i h_i + h_i \mathbf{u}_i\cdot\nabla\phi_i. \tag{A4}$$

Equations (A1)–(A4) summarize the exchanges between the main energy reservoirs of our two-layer system.

b. Time evolution of the time-mean energy reservoirs

The equations that govern the time evolution of the mean energy, derived from the definitions in (6)–(8)

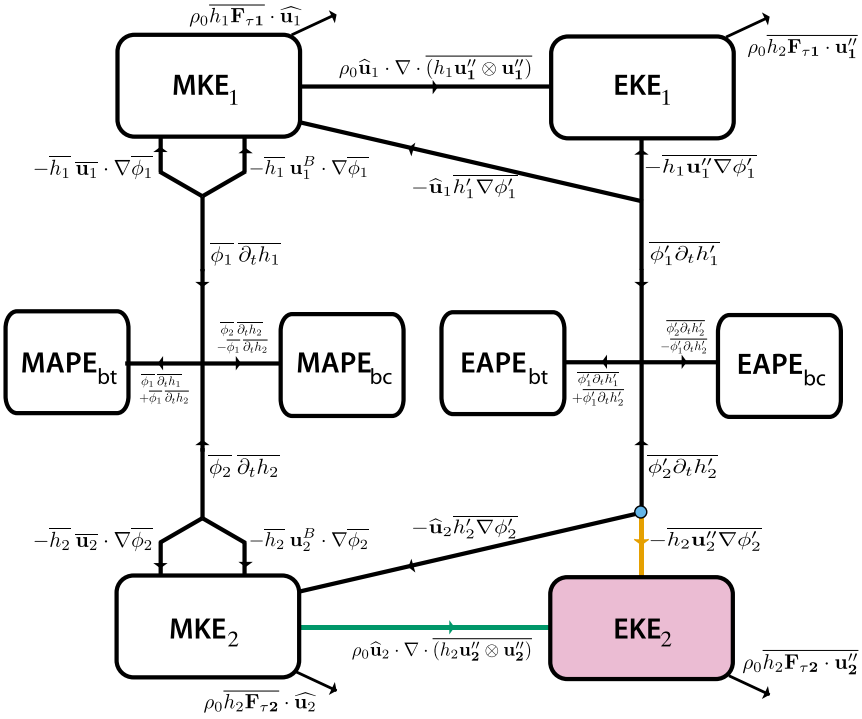

FIG. A1. Full energy diagram of our two-layer ocean based on energy equations presented in the appendix. Each energy reservoir is decomposed into mean and eddy contributions. The lines represent local conversion terms that flux energy between the reservoirs. Our results focus on examining the lower-layer EKE and the conversions to this reservoir (highlighted in color).

and a low-pass filtered version of the incompressible hydrostatic equations of motion in isopycnal coordinates (Aiki et al. 2016) are

$$\partial_t \mathrm{MAPE}_{\mathrm{bt}} = (\overline{h_1}\hat{\mathbf{u}}_1 + \overline{h_2}\hat{\mathbf{u}}_2)\cdot\nabla\overline{\phi_1} - \nabla\cdot[\overline{\phi_1}(\overline{h_1}\hat{\mathbf{u}}_1 + \overline{h_2}\hat{\mathbf{u}}_2)], \tag{A5}$$

$$\partial_t \mathrm{MAPE}_{\mathrm{bc}} = \overline{h_2}\hat{\mathbf{u}}_2\cdot\nabla(\overline{\phi_2} - \overline{\phi_1}) - \nabla\cdot[(\overline{\phi_2} - \overline{\phi_1})\overline{h_2}\hat{\mathbf{u}}_2], \tag{A6}$$

and

$$\begin{aligned}\partial_t \mathrm{MKE}_i = {} & -\nabla\cdot(\hat{\mathbf{u}}_i\mathrm{MKE}_i) - \overline{h_i}\hat{\mathbf{u}}_i\cdot\nabla\overline{\phi_i} \\ & - \hat{\mathbf{u}}_i\cdot\overline{h_i'\nabla\phi_i'} - \rho_0(\hat{\mathbf{u}}_i\cdot\nabla)\cdot\overline{(h_i\mathbf{u}_i''\otimes\mathbf{u}_i'')} \\ & + \rho_0\overline{h_i\mathbf{F}_{\tau i}}\cdot\hat{\mathbf{u}}_i, \quad (\text{for } i = 1,2).\end{aligned} \tag{A7}$$

The equation governing the mean component of the layer MP flux divergence is

$$\nabla\cdot(\overline{\phi_i}\,\overline{h_i}\,\hat{\mathbf{u}}_i) = -\overline{\phi_i}\,\overline{\partial_t h_i} + \overline{h_i}\hat{\mathbf{u}}_i\cdot\nabla\overline{\phi_i}, \quad (\text{for } i = 1,2). \tag{A8}$$

c. Time evolution of the eddy energy reservoirs

The equations governing the eddy components of energy are derived by subtracting (A5)–(A8) from the low-pass filtered version of (A1)–(A4), which govern the evolution of $\mathrm{APE}_{\mathrm{bt}}$, $\mathrm{APE}_{\mathrm{bc}}$, KE_1, KE_2, and the total MP flux divergence in each layer. Following the procedure of Aiki et al. (2016), we obtain the following equations:

$$\partial_t \mathrm{EAPE}_{\mathrm{bt}} = \overline{\phi_1'\partial_t h_2'} + \overline{\phi_1'\partial_t h_1'}, \tag{A9}$$

$$\partial_t \mathrm{EAPE}_{\mathrm{bc}} = \overline{\phi_2'\partial_t h_2'} - \overline{\phi_1'\partial_t h_2'}, \quad \text{and} \tag{A10}$$

$$\begin{aligned}\partial_t \mathrm{EKE}_i = {} & -\nabla\cdot(\hat{\mathbf{u}}_i\mathrm{EKE}_i) - \nabla\cdot(\overline{\mathbf{u}_i''\mathrm{EKE}_i}) \\ & - \overline{\mathbf{u}_i''\cdot h_i\nabla\phi_i'} + \rho_0\hat{\mathbf{u}}_i\cdot\nabla\cdot\overline{(h_i\mathbf{u}_i''\otimes\mathbf{u}_i'')} \\ & + \rho_0\overline{h_i\mathbf{F}_{\tau i}}\cdot\mathbf{u}_i'', \quad (\text{for } i = 1,2),\end{aligned} \tag{A11}$$

where $\otimes$ denotes the outer product of two vectors. The associated eddy MP flux divergence equation is

$$\nabla\cdot(\overline{\phi_i'h_i'}\hat{\mathbf{u}}_i + \overline{\phi_i'h_i\mathbf{u}_i''}) = -\overline{\phi_i'\partial_t h_i'} + \hat{\mathbf{u}}_i\overline{h_i'\nabla\phi_i'} + \overline{h_i\mathbf{u}_i''\nabla\phi_i'}. \tag{A12}$$

The full energy diagram is presented in Fig. A1.

REFERENCES

Abernathey, R., and P. Cessi, 2014: Topographic enhancement of eddy efficiency in baroclinic equilibration. *J. Phys. Oceanogr.*, **44**, 2107–2126, doi:10.1175/JPO-D-14-0014.1.

Adcroft, A., and R. Hallberg, 2006: On methods for solving the oceanic equations of motion in generalized vertical coordinates. *Ocean Modell.*, **11**, 224–233, doi:10.1016/j.ocemod.2004.12.007.

Aiki, H., X. Zhai, and R. J. Greatbatch, 2016: Energetics of the global ocean: The role of mesoscale eddies. *Indo-Pacific Climate Variability and Predictability*, S. K. Behera and T. Yamagata, Eds., World Scientific, 109–134.

Bischoff, T., and A. F. Thompson, 2014: Configuration of a Southern Ocean storm track. *J. Phys. Oceanogr.*, **44**, 3072–3078, doi:10.1175/JPO-D-14-0062.1.

Bleck, R., 1985: On the conversion between mean and eddy components of potential and kinetic energy in isentropic and isopycnic coordinates. *Dyn. Atmos. Oceans*, **9**, 17–37, doi:10.1016/0377-0265(85)90014-4.

Bracegirdle, T. J., E. Shuckburgh, J. B. Sallee, Z. Wang, A. J. S. Meijers, N. Bruneau, T. Phillips, and L. J. Wilcox, 2013: Assessment of surface winds over the Atlantic, Indian, and Pacific Ocean sectors of the Southern Ocean in CMIP5 models: Historical bias, forcing response, and state dependence. *J. Geophys. Res. Atmos.*, **118**, 547–562, doi:10.1002/jgrd.50153.

Chang, E. K. M., S. Lee, and K. L. Swanson, 2002: Storm track dynamics. *J. Climate*, **15**, 2163–2183, doi:10.1175/1520-0442(2002)015<02163:STD>2.0.CO;2.

Chapman, C. C., A. M. Hogg, A. E. Kiss, and S. R. Rintoul, 2015: The dynamics of Southern Ocean storm tracks. *J. Phys. Oceanogr.*, **45**, 884–903, doi:10.1175/JPO-D-14-0075.1.

Chen, R., G. R. Flierl, and C. Wunsch, 2014: A description of local and nonlocal eddy–mean flow interaction in a global eddy-permitting state estimate. *J. Phys. Oceanogr.*, **44**, 2336–2352, doi:10.1175/JPO-D-14-0009.1.

Chereskin, T. K., K. A. Donohue, D. R. Watts, K. L. Tracey, Y. L. Firing, and L. Cutting, 2009: Strong bottom currents and cyclogenesis in Drake Passage. *Geophys. Res. Lett.*, **36**, L23602, doi:10.1029/2009GL040940.

Downes, S. M., and A. M. Hogg, 2013: Southern Ocean circulation and eddy compensation in CMIP5 models. *J. Climate*, **26**, 7198–7220, doi:10.1175/JCLI-D-12-00504.1.

Dufour, C. O., and Coauthors, 2015: Role of mesoscale eddies in cross-frontal transport of heat and biogeochemical tracers in the Southern Ocean. *J. Phys. Oceanogr.*, **45**, 3057–3081, doi:10.1175/JPO-D-14-0240.1.

Firing, Y. L., T. K. Chereskin, and M. R. Mazloff, 2011: Vertical structure and transport of the Antarctic Circumpolar Current in Drake Passage from direct velocity observations. *J. Geophys. Res.*, **116**, C08015, doi:10.1029/2011JC006999.

Fu, L.-L., D. Chelton, P.-Y. Le Traon, and R. Morrow, 2010: Eddy dynamics from satellite altimetry. *Oceanography*, **23**, 14–25, doi:10.5670/oceanog.2010.02.

Hallberg, R., and A. Gnanadesikan, 2001: An exploration of the role of transient eddies in determining the transport of a zonally reentrant current. *J. Phys. Oceanogr.*, **31**, 3312–3330, doi:10.1175/1520-0485(2001)031<3312:AEOTRO>2.0.CO;2.

Ilicak, M., A. J. Adcroft, S. M. Griffies, and R. W. Hallberg, 2012: Spurious dianeutral mixing and the role of momentum closure. *Ocean Modell.*, **45–46**, 37–58, doi:10.1016/j.ocemod.2011.10.003.

Karsten, R., H. Jones, and J. Marshall, 2002: The role of eddy transfer in setting the stratification and transport of a circumpolar current. *J. Phys. Oceanogr.*, **32**, 39–54, doi:10.1175/1520-0485(2002)032<0039:TROETI>2.0.CO;2.

Langlais, C. E., S. R. Rintoul, and J. D. Zika, 2015: Sensitivity of Antarctic Circumpolar Current transport and eddy activity to wind patterns in the Southern Ocean. *J. Phys. Oceanogr.*, **45**, 1051–1067, doi:10.1175/JPO-D-14-0053.1.

Le Quéré, C., and Coauthors, 2007: Saturation of the Southern Ocean CO_2 sink due to recent climate change. *Science*, **316**, 1735–1738, doi:10.1126/science.1136188.

Lorenz, E. N., 1955: Available potential energy and the maintenance of the general circulation. *Tellus*, **7A**, 157–167, doi:10.1111/j.2153-3490.1955.tb01148.x.

Lu, J., and K. Speer, 2010: Topography, jets, and eddy mixing in the Southern Ocean. *J. Mar. Res.*, **68**, 479–502, doi:10.1357/002224010794657227.

Marshall, J., and K. Speer, 2012: Closure of the meridional overturning circulation through Southern Ocean upwelling. *Nat. Geosci.*, **5**, 171–180, doi:10.1038/ngeo1391.

Meredith, M. P., and A. M. Hogg, 2006: Circumpolar response of Southern Ocean eddy activity to a change in the southern annular mode. *Geophys. Res. Lett.*, **33**, L16608, doi:10.1029/2006GL026499.

Morrison, A. K., and A. M. Hogg, 2013: On the relationship between Southern Ocean overturning and ACC transport. *J. Phys. Oceanogr.*, **43**, 140–148, doi:10.1175/JPO-D-12-057.1.

Naveira Garabato, A. C., R. Ferrari, and K. L. Polzin, 2011: Eddy stirring in the Southern Ocean. *J. Geophys. Res.*, **116**, C09019, doi:10.1029/2010JC006818.

Nikurashin, M., G. K. Vallis, and A. Adcroft, 2012: Routes to energy dissipation for geostrophic flows in the Southern Ocean. *Nat. Geosci.*, **6**, 48–51, doi:10.1038/ngeo1657.

Pedlosky, J., 1963: Baroclinic instability in two layer systems. *Tellus*, **15**, 20–25, doi:10.3402/tellusa.v15i1.8825.

Rhines, P. B., 1975: Waves and turbulence on a beta-plane. *J. Fluid Mech.*, **69**, 417–443, doi:10.1017/S0022112075001504.

Rintoul, S. R., and A. C. Naveira Garabato, 2013: Dynamics of the Southern Ocean. *Ocean Circulation and Climate: A 21st Century Perspective*, G. Siedler et al., Eds., International Geophysics Series, Vol. 103, Academic Press, 471–492.

Sallée, J. B., K. Speer, R. Morrow, and R. Lumpkin, 2008: An estimate of Lagrangian eddy statistics and diffusion in the mixed layer of the Southern Ocean. *J. Mar. Res.*, **66**, 441–463, doi:10.1357/002224008787157458.

——, ——, and S. Rintoul, 2011: Mean-flow and topographic control on surface eddy-mixing in the Southern Ocean. *J. Mar. Res.*, **69**, 753–777, doi:10.1357/002224011799849408.

Sheen, K. L., and Coauthors, 2014: Eddy-induced variability in Southern Ocean abyssal mixing on climatic timescales. *Nat. Geosci.*, **7**, 577–582, doi:10.1038/ngeo2200.

Sokolov, S., and S. R. Rintoul, 2009: Circumpolar structure and distribution of the Antarctic Circumpolar Current fronts: 2. Variability and relationship to sea surface height. *J. Geophys. Res.*, **114**, C11019, doi:10.1029/2008JC005248.

Starr, V., 1968: *Physics of Negative Viscosity Phenomena*. McGraw-Hill, 254 pp.

Thompson, A. F., and K. J. Richards, 2011: Low frequency variability of Southern Ocean jets. *J. Geophys. Res.*, **116**, C09022, doi:10.1029/2010JC006749.

——, and J.-B. Sallée, 2012: Jets and topography: Jet transitions and the impact on transport in the Antarctic Circumpolar Current. *J. Phys. Oceanogr.*, **42**, 956–972, doi:10.1175/JPO-D-11-0135.1.

——, and A. C. Naveira Garabato, 2014: Equilibration of the Antarctic Circumpolar Current by standing meanders. *J. Phys. Oceanogr.*, **44**, 1811–1828, doi:10.1175/JPO-D-13-0163.1.

Vallis, G. K., 2006: *Atmospheric and Oceanic Fluid Dynamics*. Cambridge University Press, 745 pp.

Waterman, S., and S. R. Jayne, 2011: Eddy-mean flow interactions in the along-stream development of a western boundary current jet: An idealized model study. *J. Phys. Oceanogr.*, **41**, 682–707, doi:10.1175/2010JPO4477.1.

——, A. C. Naveira Garabato, and K. L. Polzin, 2013: Internal waves and turbulence in the Antarctic Circumpolar Current. *J. Phys. Oceanogr.*, **43**, 259–282, doi:10.1175/JPO-D-11-0194.1.